Engineering Structures 58 (2014) 49–62

Contents lists available at ScienceDirect

Engineering Structures

journal homepage: www.elsevier.com/locate/engstruct

Predicting the demand and plastic capacity of axially loaded steel beam–columns with thermal gradients

S.E. Quiel [a], M.E.M. Garlock [b,*], M.M.S. Dwaikat [c], V.K.R. Kodur [d]

[a] Dept. of Civil and Env. Engineering, Lehigh University, Bethlehem, PA 18015, USA
[b] Dept. of Civil and Env. Engineering, Princeton University, Princeton, NJ 08544, USA
[c] Dept. of Civil Engineering, An-Najah National University, Nablus, Palestine
[d] Dept. of Civil and Env. Engineering, Michigan State University, East Lansing, MI 48824-1226, USA

ARTICLE INFO

Article history:
Received 5 May 2010
Revised 25 July 2013
Accepted 7 October 2013
Available online 14 November 2013

Keywords:
Fire
Computational modeling
Steel
Beam–columns
Thermal gradient
Axis orientation

ABSTRACT

This study evaluates the adequacy of different methodologies to predict the plastic capacity and response caused by non-uniform thermal gradients through the depth of beam–columns that are loaded only axially at the centroid. Three models with different levels of complexity were used to evaluate the fire response of beam–columns under non-uniform temperature gradients: (1) code-based equations; (2) a fiber-beam element model; and (3) a shell element model that discretizes the full cross section and length and is capable of capturing local (i.e. plate) instability. The code-based equations do not predict the response satisfactorily since these equations do not properly consider temperature gradients. The fiber-beam element and shell model results correlate well to the thermal and structural response of the beam–columns tested experimentally with varying parameters. If local buckling is not expected at ambient temperature, complex shell elements are not necessary when the failure mode is fully plastic and fiber-beam elements, which are simpler and less "computationally expensive" than shells, suffice. The experiments and models also validated equations that consider thermal gradients and predict the plastic capacity and structural response of these members, which includes a moment reversal due to a shift in the section center of stiffness with increasing temperatures.

1. Introduction

Beam–columns are defined as members that experience a combination of axial load (P) and bending moment (M). Several types of members in steel high-rise frames under fire will act as beam–columns due to the effects of thermal expansion and thermal gradients [1]. Members that are exposed to fire on less than four sides will develop a thermal gradient through their depth, which may induce changes in the response and capacity of the member. Examples of such members are perimeter columns, which are exposed to fire on three sides, and floor beam, whose top surface is shielded by the slab. These members will experience a combination of P and M as they encounter restraint to both thermal expansion and thermal bowing in addition to their gravity loads. Thermal gradients may also produce a shift of the sections' effective centroid (i.e. the center of stiffness) away from the geometric centroid, resulting in additional bending moments for axial loads applied on the geometric centroid [1,2]. The plastic capacity of these members to resist combinations of P and M may be altered by the thermal gradients and may be conservative or non-conservative when compared to capacities calculated under the assumption of uniform temperature [3], which is the approach taken by codes [4,5].

Current practice for the fire-resistant design of steel high-rise structures typically calculates the capacity and behavior of steel beam–columns under the assumption of uniform heating [4,5]. Most numerical studies of steel beam–column behavior to date have also relied on this assumption. Numerical studies by Vila Real et al. [6] and Lopes et al. [7] examined the mechanics and capacity of wide-flanged steel beam–columns with uniform temperature, with particular emphasis on lateral–torsional buckling. The results of these studies verified the accuracy of the beam–column design requirements specified by the Eurocodes. Takagi and Deierlein [8] evaluated both the Eurocode and AISC beam–column strength design requirements with a computational study of steel beam–column performance with uniform cross-sectional temperatures. This study also validated the Eurocode approach to calculating beam–column capacity but showed that calculations according to AISC produced unconservative estimates of their lateral–torsional buckling capacity. Knobloch et al. [9] examined both the flexural and lateral–torsional buckling behavior of uniformly heated steel

* Corresponding author. Tel.: +1 609 258 2728.
E-mail addresses: squiel@lehigh.edu (S.E. Quiel), mgarlock@princeton.edu (M.E.M. Garlock), m.m.dwaikat@najah.edu (M.M.S. Dwaikat), kodur@egr.msu.edu (V.K.R. Kodur).

0141-0296/$ - see front matter © 2013 Elsevier Ltd. All rights reserved.
http://dx.doi.org/10.1016/j.engstruct.2013.10.005

beam–columns with a parametric numerical study of different combinations of axial load and moment. Eurocode standards for fire-exposed steel beam–columns were shown to be conservative for most cases of lateral–torsional buckling but not always for flexural buckling.

Few studies have addressed the performance of steel beam–columns that develop a thermal gradient through their depth due to non-uniform heating. Takagi and Deierlein [8] noted that the uniform temperature approach to calculating the performance of steel beam–columns may be unconservative for members in which a thru-depth thermal gradient develops. Wang et al. [10] computationally examined the performance of axially and rotationally restrained steel columns under fire that developed thermal gradients through their depth and thus acted as beam–columns. Significant bending moments were induced by the thermal gradient through the depth of the members. However, the exact mechanics that produced these moments, as well as the gradient-induced changes in plastic capacity were not explicitly discussed. The plastic capacity of these members to resist combinations of P and M was also not addressed.

Each of these previous studies has expressed the need for experimental testing of fire-exposed steel beam–columns to further validate existing computational methods to calculate their performance. In this paper, the results of recent fire tests on beam–columns are utilized to evaluate the ability of different methodologies to predict the performance of the steel beam–columns with thermal gradients. The specimens are columns that are axially loaded at the centroid, with no lateral loads (the moment is induced entirely by the thermal gradients). The fire tests were conducted at the Center for Structural Fire Engineering and Diagnostics at Michigan State University (MSU) in collaboration with Princeton University. The results of these fire tests experimentally confirmed the unique behavior and capacity demonstrated by steel beam–columns with thermal gradients described by Garlock and Quiel [2,3].

The objective of this study is to evaluate the adequacy of different methodologies to predict the capacity and response caused by non-uniform thermal gradients through the depth of beam–columns. Three models with different levels of complexity were used to evaluate the fire response of beam–columns under non-uniform temperature gradients: (1) code-based equations; (2) a fiber-beam element model; and (3) a shell element model that discretizes the full cross section and length and is capable of capturing local (i.e. plate) instability. Such an evaluation has not been done in the past and it will assist engineers in understanding the adequacies and shortcomings of each methodology.

2. Fire resistance tests

To generate data for validation of computer models, four beam–column specimens were tested by exposing them to fire. The fire resistance tests on steel beam–columns were carried out using a structural fire testing furnace recently commissioned at Michigan State University. Fig. 1 shows the furnace and a schematic of the test setup. The furnace is capable of simulating and monitoring both standard and design fire scenarios. The experimental program consisted of fire resistance tests on four steel columns designated C1-S, C1-W, C2-S, and C2-W with test parameters as shown in Table 1. Specimens C1-S and C1-W were tested simultaneously in the furnace, as were Specimens C2-S and C2-W. All specimens were a W8x48 cross-section with A992 Grade 50 steel (F_y = 345 MPa) and were fabricated to a length of 3.3 m.

The average measured dimensions of each specimen with their corresponding insulations schemes and thicknesses are shown in Figs. 2 and 3. As seen in Fig. 2, the top and bottom ends of each specimen, which were not to be exposed to fire, were left unprotected. The insulation material that was used is CAFCO 300 with physical properties as shown in Table 2 [11]. Fig. 3 shows the insulation thickness and thermal discretization of the cross-section. Since the columns were exposed to fire from four sides, the insulation was removed in specific locations, as shown in Figs. 2 and 3, to create a thermal gradient in the desired direction. The insulation thickness values in Table 1 are the average values for each beam column specimen. The average values are calculated from measurement at three different sections on the specimen. At least 10 perimeter readings of actual insulation thickness were recorded at each section. The insulation thickness was intended to provide at least 2 h of fire rating (according to prescriptive approaches). More details on this matter can be found in [12].

The beam–columns, which were fixed in all degrees of freedom at the bottom and partially rotationally and axially restrained at the top, were subjected to a constant axial load at the top and then exposed to two types of fire scenarios. Table 1 shows the test matrix used in these fire tests. The specimens were monitored during the test and several quantities were recorded in real time, such as steel and furnace temperatures at various sections, total strains at the base of every column, rotation and vertical displacement at the top of every column, the fire induced axial force in every column. Detailed description and results of the fire tests can be found in Dwaikat et al. [12].

3. Predictive models

The data from the fire tests is used to evaluate the results of computational modeling of the experimental specimens. Three types of models are considered in this study: the *code-based* model, the *fiber-beam element* model, and the *shell* model. The code-based models are based on European and American Standards [4,5]. The fiber-beam element model uses beam elements where the cross-section is subdivided into fibers as shown in Fig. 3 (which shows the four experimental specimens). The temperature of each fiber is calculated via computational thermal analysis of the discretized cross-section. These temperatures are then used as input for the structural analysis, which considers each fiber to have individual stress, strain, and temperature-dependent material properties. By using fiber-beam elements, the thermal gradients can be captured, whereas in a common beam element only a uniform temperature can be assumed. The *shell element* model can also capture thermal gradients and in addition it can capture local (i.e. plate) instability. A detailed description of these three models follows.

3.1. Code-based model

The code-based model is not a 'model' per se but a code-based methodology for solving both the capacity and demand imposed on perimeter columns with thermal gradients.

The American AISC Code [5] permits the use of one-dimensional heat transfer (e.g., a lumped mass approach) to calculate the thermal response in beams and columns, in which case thermal gradients are not considered. For calculating the *capacity* of beam–columns, it does not consider how the interaction of axial load and moment changes, and neither does the European Eurocode [4]. Garlock and Quiel [3] have shown that the axial load – moment interaction changes when thermal gradients are present. For example, Fig. 4 shows the combined axial load (P) and moment (M) capacity of a wide flanged section normalized by the yield axial force (P_y = area times the yield stress) and the plastic moment capacity (M_p = plastic section modulus times the yield stress), respectively. This Fig. shows that if the thermal gradients are neglected, the shape of the capacity envelope approximates a

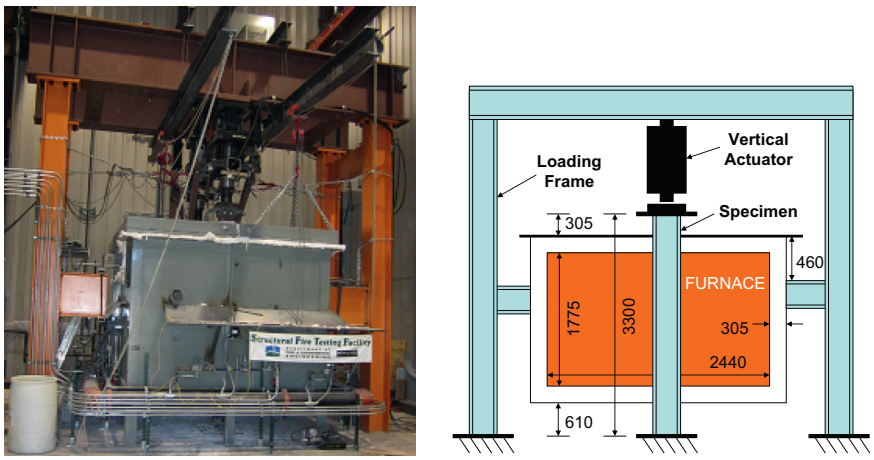

Fig. 1. Structural-fire test furnace at MSU's Civil and Infrastructure Laboratory and schematic of the test setup.

Table 1
Summary of fire test parameters.

Specimen	Fire exposure	Axis orientation	SFRM thickness (mm)	Initial $\frac{P}{P_y}$
C1-S	ASTM E119	Strong	44	0.25
C1-W	ASTM E119	Weak	44	0.25
C2-S	Design fire	Strong	38	0.45
C2-W	Design fire	Weak	38	0.45

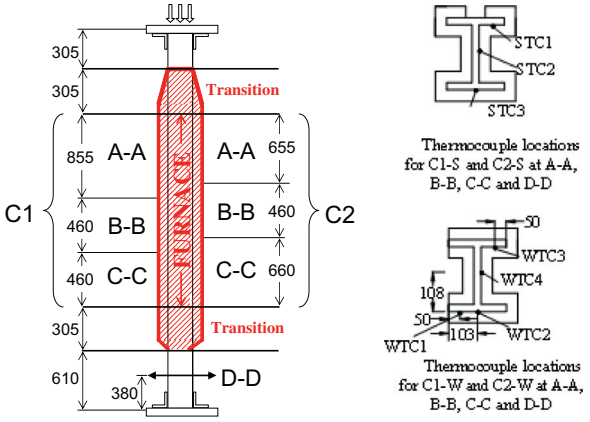

Fig. 2. Temperature zones for the direct validation model and thermocouple locations.

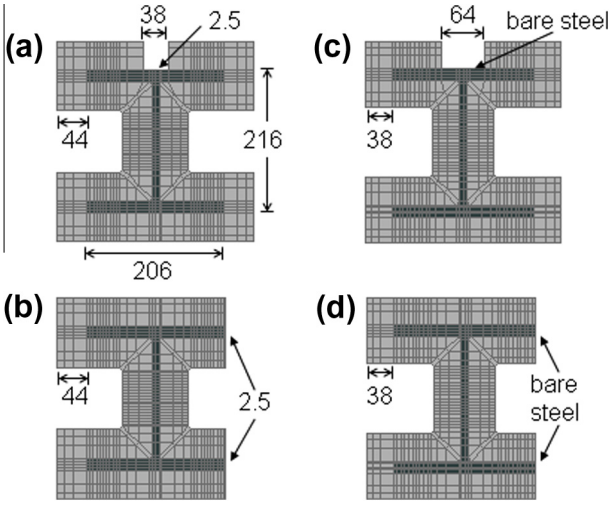

Fig. 3. Discretized cross-sections of (a) C1-S, (b) C1-W, (c) C2-S, and (d) C2-W used for blind calculation thermal analysis in SAFIR.

diamond shape. This is the shape of the envelope that both the European and American code equations approximate for elevated temperature combined P and M capacity. However, Fig. 4 shows that if a thermal gradient is present, the shape of that capacity envelope changes. The shaded area represents combinations of P and M that are acceptable per the American and European codes, but in reality the section has failed (it has exceeded its P–M capacity) for combinations of P and M in that region.

In addition, the codes do not provide guidance for the moments that are induced by the thermal gradients if the member is rotationally restrained. Garlock and Quiel [2] have shown that the moments induced by that gradient and the shift in the effective centroid (center of stiffness) of that section produces moments that should not be neglected. These are important considerations for calculating the moment *demand*, M, which should also consider the effects of the adjacent structure that can also impose moments.

Full section yielding under combined P and M is one limit state (reaching of capacity) that leads to failure but there can be other limit states that lead to failure beforehand such as overall buckling and local buckling. Takagi and Deierlein [8] evaluated both the Eurocode and American codes for overall buckling under uniform temperature (no thermal gradients) and found that the American code significantly overestimates the strength of sections under combined P and M, while the European code is more accurate. Quiel and Garlock [13] have recently evaluated both codes for local plate (flange and web) buckling based on finite element simulations and came to the same conclusion: the American code severely overestimates the capacity of plates at elevated temperature and the Eurocode provides a good approximation but only for larger values of the non-dimensional slenderness ratio, which is modified for temperature T ($\lambda_{c,T}$). An example of this trend is shown in Fig. 5, which predicts the critical buckling stress (F_{cr}) normalized by the yield stress (F_y) for a stiffened plate (pinned on both ends) uniformly loaded at a temperature of 500 °C. Both codes are plotted as is the finite element solution and a predictive equation proposed by Quiel and Garlock. In the shell model section of this paper we will use these predictive equations to estimate if we expect local buckling.

Table 2
Thermal properties used for CAFCO 300.

Temperature (°C)	Thermal conductivity (W/m K)	Specific heat (J/kg K)	Density (kg/m^3)
20	0.078	900	310
1200[a]	0.3[a]	1400[a]	310[a]

[a] Assumed values based on previous experimental data.

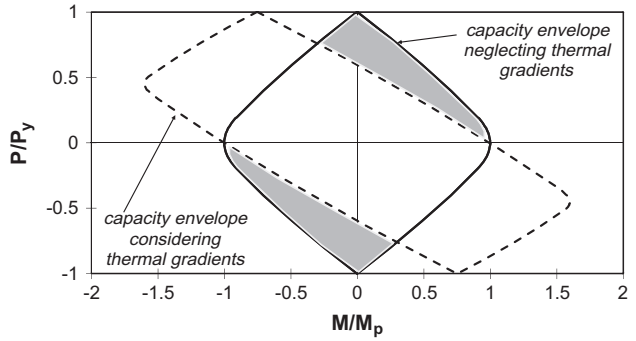

Fig. 4. Combined axial load (P)–moment (M) capacity diagram normalized by the axial yield force (P_y) and the plastic moment capacity (M_p): comparison of diagram with and without thermal gradients.

3.2. Fiber-beam element model

Two types of fiber-beam element models were used in this study: (1) The *forensic fiber* model provides a direct validation of the experiments using experimentally obtained temperatures, loading, and boundary conditions as inputs to a computational structural model; and (2) the a priori *fiber* model is a blind calculation of both thermal and structural performance. The latter model uses idealized inputs meaning nominal specimen dimensions, idealized boundary conditions (pinned, fixed), and an approximate fire time–temperature curve to provide an estimate of thermal and structural performance. Comparing the results of a priori fiber model with those of the forensic fiber model and the experimental data demonstrates the accuracy to which computational analysis using idealized inputs and conditions can predict the actual performance of fire-exposed steel beam–columns.

SAFIR, a software specifically designed for the analysis of structures exposed to fire [14], was used for this study to perform uncoupled thermal and structural analyses. In the thermal analyses, the cross-section of each member is discretized into several elements (fibers), and a user-defined fire is imposed on the appropriate boundaries. The output is a time–temperature history at every fiber of the member's cross-section. These temperatures are used to construct the member's cross-sectional temperature profile, which is then used to calculated mechanical response using either three-noded fiber-beam elements or multi-layered shell elements that are solved using four Gaussian integration points across its surface. The latest version of SAFIR offers the capability of a dynamic analysis using a modified version of the Newmark-beta method, which allows the program to continue its solution beyond the point at which material or geometric instabilities may emerge [14]. Since the governing equation includes the mass of the structure, the solution is capable of withstanding local instabilities and large deflections.

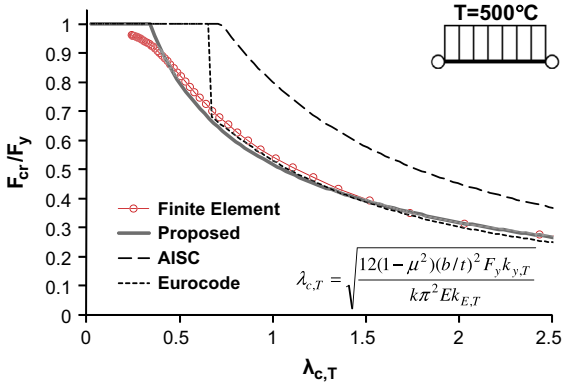

Fig. 5. Critical buckling stress (F_{cr}) normalized by the yield stress (F_y) for a uniformly loaded plate at 500 °C with pin boundary conditions on both ends. Shown as a function of the non-dimensional slenderness ratio $\lambda_{c,T}$.

In the fiber-beam element models used for this study, the 3.3-m length of the column is divided into 64 elements, resulting in a 50-mm discretization. This discretization is based on an optimization study where larger discretization did not yield different results. Structural material properties at elevated temperature for steel were based on Eurocode [4], and the ambient yield strength of the ASTM A992 steel was approximated as 345 MPa.

Residual stresses are not considered in any computational model used for this study because relaxation of initial residual stresses is likely to occur in fire-exposed steel members due to an increase in steel temperature [15]. In an experimental study of the strength of wide-flanged columns at elevated temperature, Yang et al. [16] have shown that initial residual stresses had significantly less effect on local and global buckling failure modes than at ambient temperature. Heidarpour and Bradford [17] showed similar results in a separate parametric computational study of residual stress effects in heated steel members. Global geometric imperfections were also not included in the computational models because their effects were considered to be outside the scope of this research effort. The beam–columns used for the experiments on which this computational study is based were purposefully selected to experience plastic failure and therefore had little if any initial out-of-straightness. Neglecting initial global imperfections in this case is therefore justified, but a parametric analysis of the effects of this type of imperfection on fire-exposed steel beams–columns that develop thermal gradients would be warranted in a separate future study.

The length of the member passing through the furnace is divided into three heated zones (A–A, B–B, and C–C) as shown in Fig. 2, where the thermocouples are located at the center of each zone [12]. The 305-mm "transition" lengths just outside the top and bottom of the furnace use thermal profiles with linearly decreasing temperatures over that length from the hot steel temperatures at A–A and C–C, respectively, to room temperature. The ends of the member beyond the transition zones are therefore modeled as cool.

Fig. 2 shows the distribution of thermocouples on the column as recorded in the experiments and used for the forensic fiber model. Since the forensic fiber model is used to reproduce experimental specimen performance as accurately as possible, the precise experimental thermal and boundary conditions are input. The cross-sectional thermal profiles for these analyses were constructed using thermocouple temperature data recorded during the experiment reported in Dwaikat et al. [12]. For the "strong axis specimens" (i.e. the specimens with thermal gradients parallel to the web), each flange is assumed to have constant temperature through its thickness and across its width. These temperatures are equal to those recorded by the thermocouples in the experiments. The temperature of the web is then obtained by linearly interpolating between the flange temperatures and the temperature recorded at the middle of the web. For the "weak axis

specimens" (i.e. the specimens with gradients parallel to the flanges), linear interpolation is used to obtain temperatures between thermocouples. Extrapolation using the same linear relationships is used to project the temperature profile in the flange tips beyond the range of the thermocouples. Examples of these piecewise linear thermal distributions are shown in Fig. 6a and b for a strong axis section and weak axis section.

For the a priori model, the thermal profile was obtained via thermal analysis of the cross-section in SAFIR. The discretized cross-sections used for thermal analysis of these specimens are shown in Fig. 3. The CAFCO 300 SFRM insulation applied to each specimen was modeled with the nominal thickness prescribed by the original experimental setup (i.e. 44 mm for the C1 columns and 38 mm for the C2 columns). Thermal material properties for CAFCO 300 used for the a priori model are shown in Table 2. The properties at room temperature are provided by Isolatek International's brochure for CAFCO 300 [11]. For insulation material the thermal conductivity and heat capacity generally increase with temperature [18]. Thermal conductivity and specific heat were modeled as increasing linearly from their values at room temperature to higher values at 1200 °C shown in Table 2. These values were selected as a conservative estimate based on research performed at the National Institute of Standards and Technology (NIST) on the temperature-induced variation of thermal properties in several SFRM's similar to CAFCO 300 [19]. Thermal properties for steel were based on Eurocode [4].

Thermal analyses were not necessary for the forensic fiber models since nodal temperatures were based on experimental data as described previously. The a priori models, however, required a thermal analysis and therefore a thermal input (i.e. a fire time–temperature curve). The C1 columns were subjected to the ASTM E119 standard fire curve, and the C2 columns were subjected to a design fire that followed the ASTM E119 curve until $t \sim 90$ min at which time a rapid decay to room temperature was invoked. Over the majority of the section, the convective heat transfer coefficient, h, and relative emissivity, ε, for the fire-exposed surfaces were assumed to be 25 W/m^2 K and 0.8, respectively. The exposed surfaces in the insulation gaps in the strong axis sections were modeled with decreased h and ε values of 10 W/m^2 K and 0.2, respectively, because these surfaces are partially shielded from fire exposure. Examples of the realistic thermal profiles resulting from these analyses are plotted in Fig. 6a and b, which show that these distributions agree reasonably well with the piecewise linear temperature distributions used for the forensic fiber model.

The boundary conditions, loading, and gradient orientation used for the fiber models are shown in Fig. 7. The bottom end of each specimen is modeled as fixed to approximate the bolted angle connection used in the experiment. Vertical and rotational linear springs represent the resistance to thermal expansion and thermal bowing provided by the piston-to-plate connection. In the forensic fiber models, the rotational spring was represented by a freely rotating pin to which the experimental rotations were applied. Similarly, the vertical spring in Fig. 7 was approximated by directly applying the experimentally measured axial load, which varies due to the resistance of the loading frame against vertical thermal expansion, to the top end of the model specimen. Experimental data indicated that the top end did not translate laterally, therefore the columns are modeled as having no top-end translation. In the a priori models, instead of inputting the measured rotation and displacement at the top of the column, we used vertical and rotational springs. The magnitudes of stiffness for the vertical spring, k_s, and the rotational spring, k_θ, were estimated to be 25,000 kN/m and 2500 kN - m/rad, respectively, based on the vertical and rotational stiffnesses recorded during the experiments reported by Dwaikat et al. [12].

3.3. Shell element model

The advantage to a shell model is that it can capture local buckling whereas the fiber models discussed previously cannot. Quiel and Garlock [13] performed an extensive computational study to predict the critical buckling stress of plates with various boundary conditions, loading, and temperature. Since they found the American and European codes to inadequately predict plate buckling, they proposed their own predictive equations (see Fig. 5). Based on their proposed equations, Table 3 lists the values of the critical buckling stress (F_{cr}) normalized by the yield stress (F_y) for seven different boundary condition and loading cases for the flanges and web of the W8x48 specimen heated to four different temperatures. The 'real' boundary conditions of the plates are somewhere between pinned (e.g., cases 1 and 4) and fixed (e.g., cases 2 and 5). Values of F_{cr}/F_y equal to one means that the plate (flange or web) will yield before it buckles. The table indicates that except for Cases 1 and 4, plate yielding controls over plate buckling for temperatures less than 500 °C. Recent research [20] has shown that Cases 1 and 4 are not good representations of the web and flange restraint in an I-shape assembly (the boundary conditions are closer to fixed). Therefore, we assume that local buckling does not control the failure limit state for temperatures less than 500 °C. At temperatures higher than 500 °C, the F_{cr}/F_y values start to become less than one, which means that if the temperature in the plates exceed this value, it is possible that local buckling will control the failure limit state.

To examine if local buckling would develop during the experiments, a shell element model of each specimen was developed

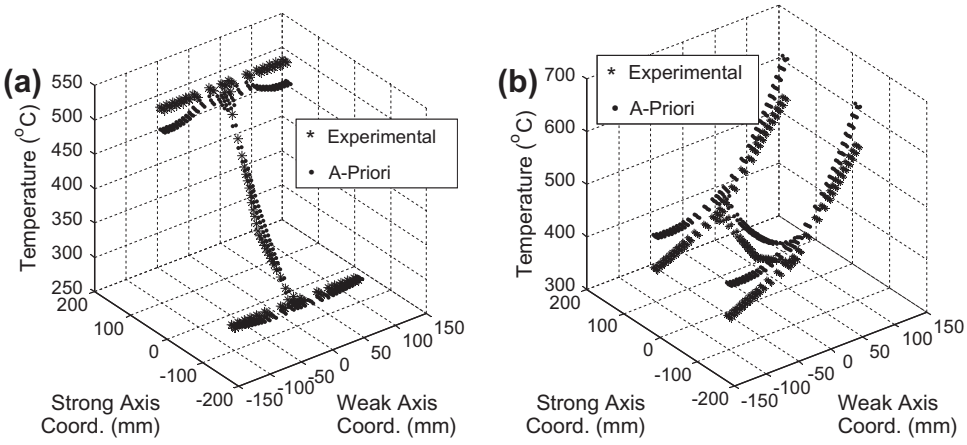

Fig. 6. Plot of cross-sectional temperature distribution at $t = 30$ min for (a) C2-S and (b) C2-W.

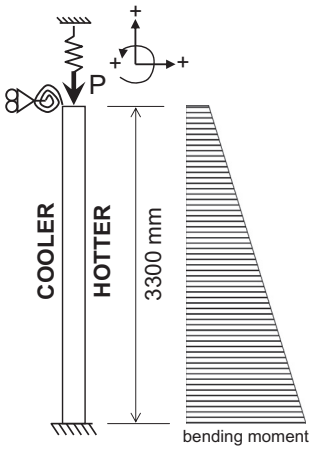

Fig. 7. Column orientation, boundary conditions, and moment distribution.

and analyzed. The shell element model can be directly compared to the forensic fiber model since both use the same boundary conditions, loading, and thermal inputs. This model used four-noded shell elements in SAFIR with approximately a 50-mm by 50-mm square discretization per shell (i.e. with 64 shells over the length of the 3.3-m member) based on an optimization study. Initial local geometric imperfections were included in both the web and flanges in order to realistically model the potential for local buckling. These imperfections were modeled as sinusoidal with the same wavelength as the lowest buckling mode obtained from linear analysis of the plates at ambient temperature. The maximum magnitude of the imperfection was modeled as the plate width (d for the web and $b_f/2$ for the flange) divided by 200. A literature review of several studies of local buckling in fire-exposed steel plates was previously conducted by the authors [13], and the maximum imperfection magnitude was obtained from the results of that review.

4. Comparison of results

The thermal and structural analysis results from the code-based model, the fiber-beam models (both forensic and a priori), and shell element model are compared to the fire tests data reported in Dwaikat et al., [12]. The thermal response, structural response, and plastic response at failure are examined below.

4.1. Thermal response

Fig. 8 compares the temperatures recorded by the thermocouples at section B–B for each of the four columns to the temperature calculated via computational thermal analysis of the a priori fiber model's fire-exposed cross-section. The B–B cross-section was selected for this comparison because it consistently recorded the highest temperatures for each specimen due to its location in the middle of the furnace and therefore represents the worst case scenario for temperature increase [12].

In Fig. 8a and b, the a priori fiber model temperatures for columns C1-S and C1-W are initially conservative because the computational thermal model does not account for the evaporation of the insulation's residual water near 100 °C, which slowed the initial increase of temperature. Temperature variation between the computational and experimental results throughout the time series may also have been caused by variation in the actual SFRM thickness as compared to the idealized constant 45-mm thickness used for computational thermal analysis [12].

Despite some initial variation, the a priori fiber model temperatures for columns C1-S and C1-W reached similar maximum temperatures as the thermocouple measurements. It can be seen in Fig. 8a and b that at around $t \sim 200$ min. specimens C1-S and C1-W underwent a rapid increase in recorded temperatures greater than that predicted by the a priori fiber model. This rapid increase in recorded temperature can be explained by the emergence of cracks in the insulation and the loose breakage of a few fragments of insulation prior to failure. These cracks and breaking of insulation layer can be attributed to the increasing deflections and increasing fragility of the insulation at high temperature. The damaged insulation, as shown in Fig. 9a for specimen C1-S at $t \sim 200$ min, would then allow a faster increase of the section's temperature.

Fig. 8c and d show even better agreement between experimental and a priori fiber model temperatures for columns C2-S and C2-W throughout the time series. Both the experimental data and the

Table 3
F_{cr}/F_y values (based on proposed predictive equations [13]) for the W8x48 flange and web plates with varying boundary conditions, loading conditions, and temperatures.

Case No.	Loading and boundaries	T = 300 °C	T = 500 °C	T = 600 °C	T = 700 °C
Stiffened (Web)					
1		1.00	0.93	0.78	0.79
2		1.00	1.00	0.85	0.87
3	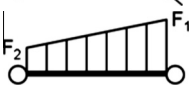	1.00	1.00	0.85	0.87
Unstiffened (Flange)					
4	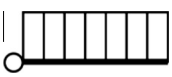	1.00	0.89	0.75	0.76
5		1.00	0.99	0.84	0.85
6	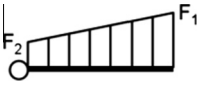	1.00	1.00	0.92	0.93
7	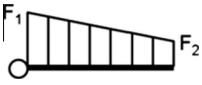	1.00	1.00	0.95	0.97

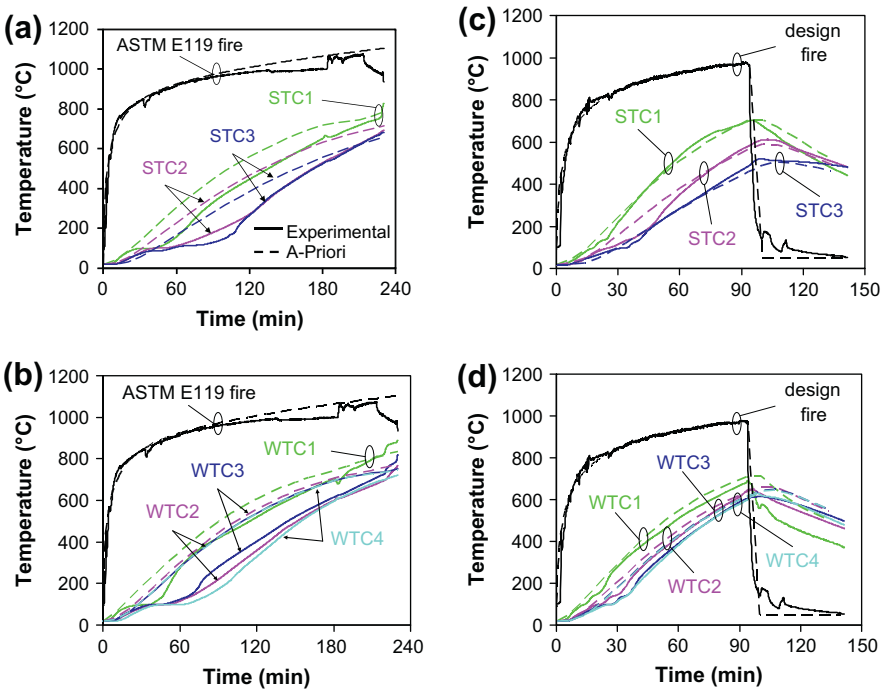

Fig. 8. Comparison of experimental and blind calculation temperatures for (a) C1-S, (b) C1-W, (c) C2-S and (d) C2-W.

a priori fiber models experience similar temperature increase as the fire intensifies, reach similar maximum temperatures, and undergo similar decrease in temperature during the decay phase. The magnitude of the thermal gradients due to heating and the reversal of these gradients during the decay phase were also similar. The fire protection for both specimens experienced only minimal cracking, as shown in Fig. 9b for specimen C2-W at $t \sim 100$ min, thus preventing either a sudden increase in experimental temperature during peak exposure or a more rapid temperature decrease during the decay phase.

4.2. Structural response

The results of computational structural analysis for both fiber-beam models (forensic and a priori) are compared to experimental data for all four columns in Figs. 10–13. The figures show (a) axial deformation, (b) top-end rotation, (c) the axial load applied to the member, and (d) the bending moment measured at section D–D as a function of time. Figs. 10a–13a show that the axial displacement trends of the computational models are similar to those of all four experimental specimens. Furthermore, both models provide a conservative estimate compared to values recorded during the fire tests. Computational axial displacements are roughly 30–40% greater than experimental values, most likely due to the use of Eurocode properties to model the structural behavior of steel. A recent report by researchers at NIST on the fire-exposed properties of structural steel [21] shows that the coefficient of thermal expansion for steel is less than that specified by Eurocode. Therefore, using (conservative) Eurocode values to calculate the thermal expansion of actual specimens likely contributed to the overestimation of axial displacement in Figs. 10a–13a.

Note that the (b) and (c) plots in Figs. 10–13 show that the curves representing top end rotation and axial load, respectively, for the forensic fiber models and the experimental data are identical. Since the a priori fiber model thermal analyses adequately predict the increases in steel temperature measured during the fire tests, the (b) and (c) plots in Figs. 10–13 can be used to evaluate the accuracy of the rotational and vertical springs used in the a priori fiber structural model. These plots show that the spring stiffnesses used in the a priori fiber model were able to reasonably predict the trend and magnitude of top-end rotation and change in axial load that result from the resistance of the loading frame to thermal expansion and thermal bowing. The a priori fiber model rotations increase earlier in the time series because the growth of their thermal gradients is not slowed by the evaporation of residual water in the insulation.

Figs. 10d–13d show the moment curves for each of the two computational models as well as the experimental moments [12]. These plots show similar moment trends for both computational models and the experimental data among all four specimens. All data sets show an initial increase in positive moment due to restraint of thermal bowing, followed by a shift of the effective centroid (i.e. the center of stiffness) which produces a moment reversal. For columns C1-S and C2-W (Figs. 10d and 13d), the moments at D–D obtained from the forensic fiber model show close agreement with those obtained from experimental data. This correlation indicates not only that the strain gauge data for these

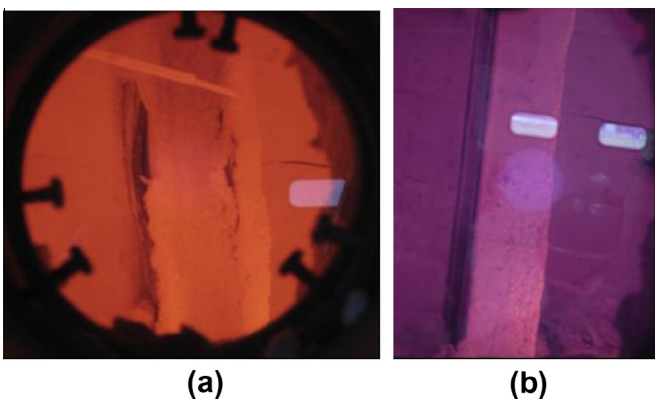

Fig. 9. Photos of specimen (a) C1-S at $t \sim 200$ min, and (b) C2-W at $t \sim 100$ min during the fire tests.

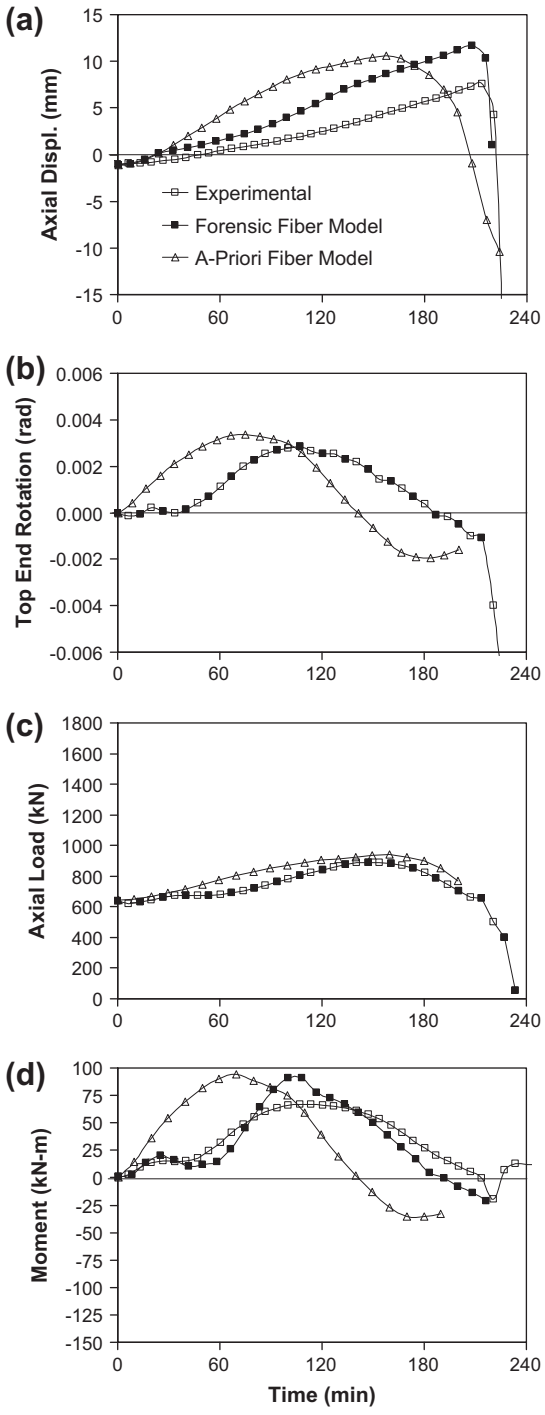

Fig. 10. Plots of (a) vertical axial displacement, (b) top end rotation, (c) axial load, and (d) moment at D–D for beam–column C1-S.

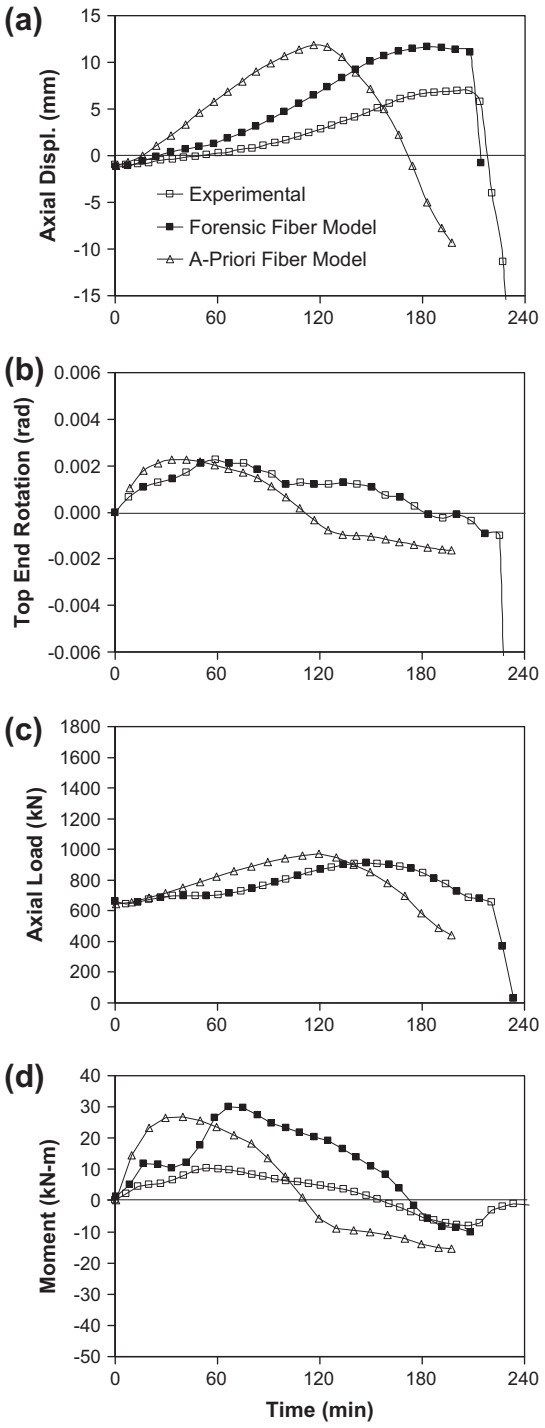

Fig. 11. Plots of (a) vertical axial displacement, (b) top end rotation, (c) axial load, and (d) moment at D–D for beam–column C1-W.

specimens is reliable but also that the structural analysis performed with the forensic fiber model is able to accurately predict the development of bending moment caused by the experimentally measured thermal gradient. The a priori fiber model moment for C1-S also shows similar magnitudes of positive and negative bending moment as the forensic fiber model and experimental data.

The a priori fiber model for specimen C2-W (Fig. 13d) shows similar trends in overall moment and similar magnitudes of negative moment but a different magnitude of positive moment. This variation is caused by a difference in thermal gradient over the thru-furnace length of the column between the experiment (and therefore forensic fiber model) and the a priori fiber model. The thermal gradient in section C–C recorded during the fire test for column C2-W was much smaller than the gradient at A–A and B–B [12]. The C–C experimental gradient was also small compared to the thermal gradient obtained from a priori fiber thermal analysis, which was applied to the entire heated length of that model. Since the experimental specimen and the forensic fiber model have a shorter length with a significant gradient, they developed smaller magnitudes of positive bending moment in response to thermal bowing. Likewise, both the experimental and forensic fiber cases

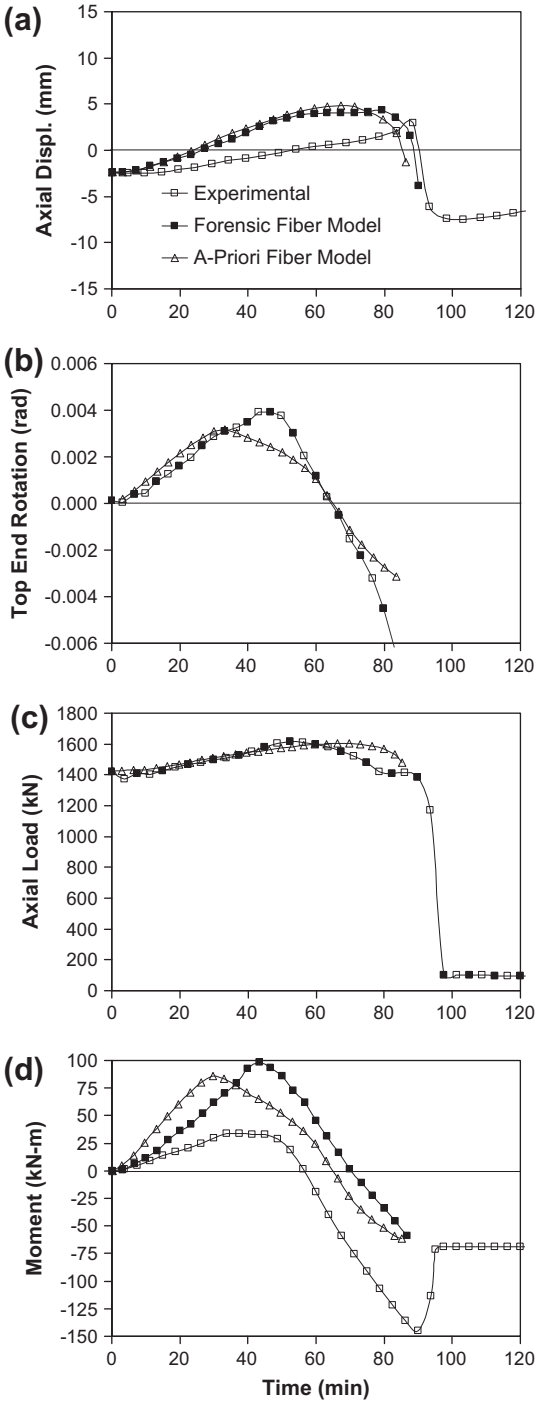

Fig. 12. Plots of (a) vertical axial displacement, (b) top end rotation, (c) axial load, and (d) moment at D–D for beam–column C2-S.

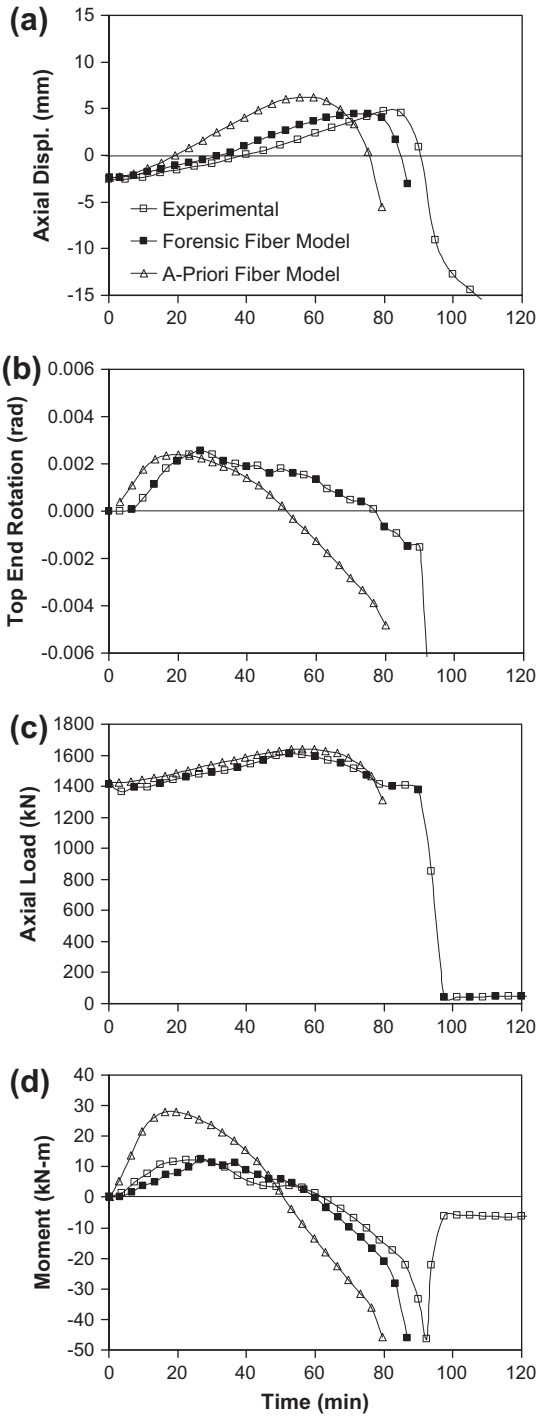

Fig. 13. Plots of (a) vertical axial displacement, (b) top end rotation, (c) axial load, and (d) moment at D–D for beam–column C2-W.

also experienced a smaller moment reversal than the a priori fiber model because they have a shorter length over which the effective centroid has shifted. However, when the negative moments that cause the reversal are added to the positive moments, the end result, which is the maximum negative moments at failure, is the same for all cases.

For specimens C1-W and C2-S (Figs. 11d and 12d), the trend of moments at D–D is similar for all three data sets. However, only the two computational models show overall agreement in magnitude. Experimental moments for C1-W, though reaching similar values of negative moment, experienced positive moments up to three times smaller than that of the computational models.

Table 4
Recorded times (in minutes) to column failure.

Specimen	Experiment	Fiber-beam models		Shell model
		Forensic	A-priori	Forensic
C1-S	220	219	198	210
C1-W	215	212	197	196
C2-S	90	89	85	85
C2-W	93	87	80	82

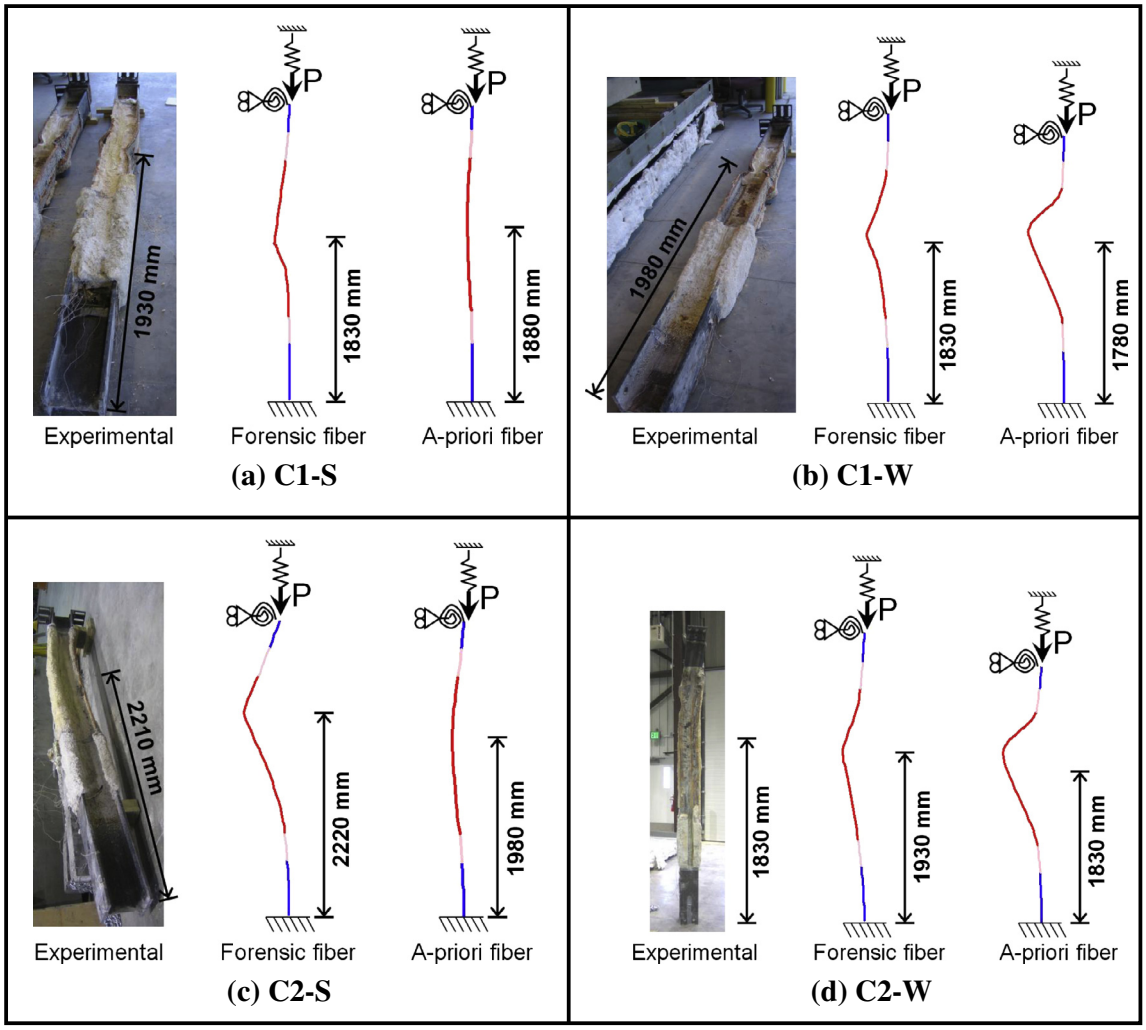

Fig. 14. Failure patterns of beam–columns (a) C1-S, (b) C1-W, (c) C2-S, and (d) C2-W after fire tests.

Table 5
Steel temperature at failure and time to failure based on American and European codes.

Specimen	American AISC			European Eurocode		
	Steel Temp (°C)	Time (min)		Steel Temp (°C)	Time (min)	
		LM[a]	HTA[b]		LM[a]	HTA[b]
C1-S	672	80	159	654	78	152
C1-W		83	143		80	136
C2-S	577	54	70	561	52	68
C2-W		66	65		64	62

[a] Lumped mass one-dimensional analysis.
[b] Heat transfer analysis where maximum temperature is used (see Fig. 8, A-Priori results).

Positive experimental moments for C2-S showed a similar variation, and negative moments were up to times greater in magnitude. Since the two computational models showed reasonable overall agreement, it is possible that the strain gauge data is not reliable for these specimens. For example, there may have been slip at the interface of the gauges and the steel, mechanical problems with the gauges, or experimental error.

4.3. Structural failure based on computational models

Despite some variation in moment magnitude between the experimental results and the two computational results, Table 4 shows good agreement between the predicted failure times of the computational models and the measured failure times of the experiments. Failure in computational structural analysis is defined as the last time step (prior to instability) at which convergence was achieved. This event occurs when the column can no longer carry its loads. As seen in Table 4, the time to failure for every specimen gets progressively more conservative when comparing the experimental results to the forensic fiber model results to the a priori fiber model results.

Fig. 14 compares a photograph of the failed tested column to the fiber-beam models (forensic and a priori) deformation at the end of the analysis. The photographs seem to show 'buckling' of

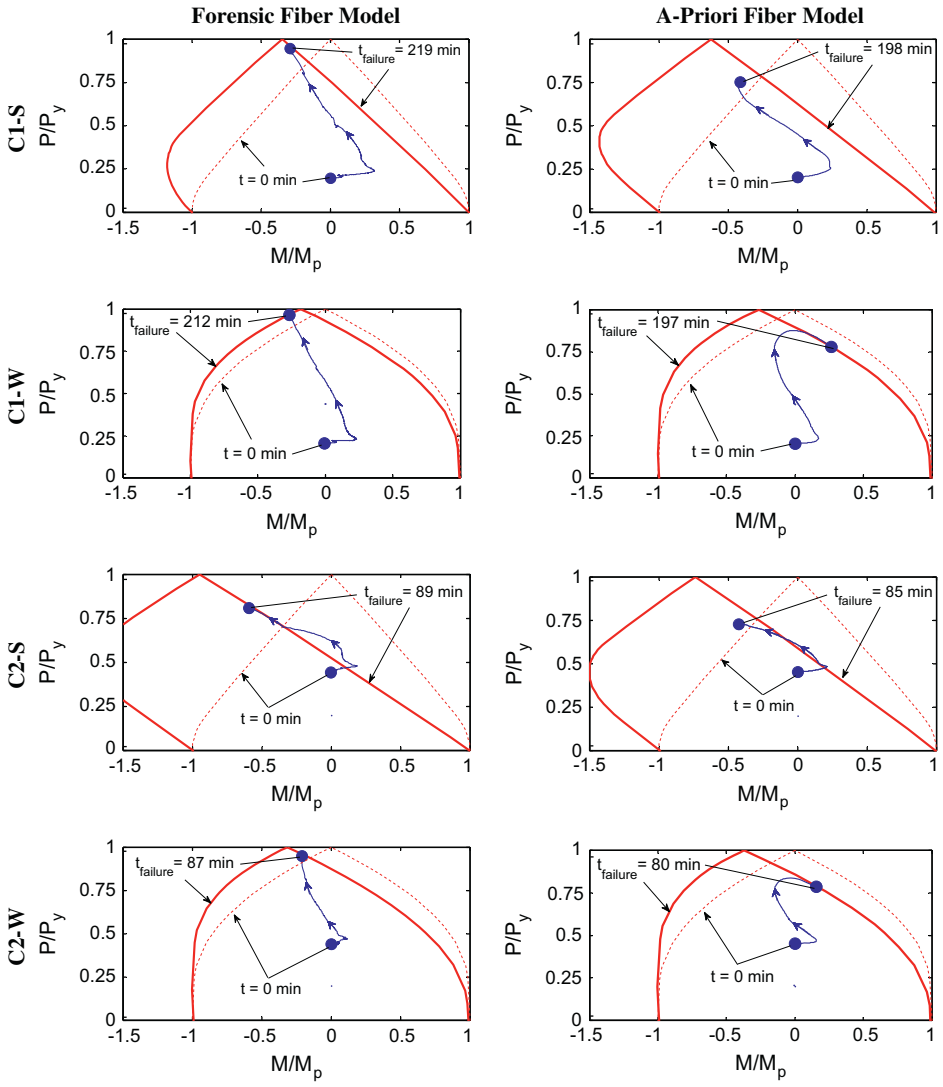

Fig. 15. Plastic *P–M* capacity diagrams for the computational fiber-beam element models of each beam–column.

the flange and web plates, however this 'buckling' was likely squashing of the plates after the full section yield and not a local instability. The next sections provide data and discussion to support this theory.

The experimental and computational results in Fig. 14 show good agreement on the location of failure along the length of the column. Note that the locations of failure do not correspond to the point of largest moment and lowest capacity along the members' heated length. The hottest region (i.e. with the least capacity) on the experimental specimens roughly spanned from the middle of the B–B zone to the middle of the A–A zone shown in Fig. 2 (i.e. in the approximate range of 1500–2300 mm measured from the bottom of the column). The hottest region on the forensic fiber model was similar. Since under thermal gradient each column had a moment distribution similar to that shown in Fig. 7, one would have expected plastic failure at the bottom of these regions where moments were largest. Likewise, one would have expected the a priori fiber models to have failed near the bottom of the furnace (at a height of ~915 mm). However, the failed shapes in Fig. 14 show that critical points for all cases emerged at locations of smaller moment, and this phenomenon can be explained by examining each section's combined axial load (P) and moment (M) demand and plastic capacity, both of which are affected by the thermal gradients and change with time.

4.4. Code-predicted failure times

The American AISC Code permits one-dimensional heat transfer analysis (e.g., lumped mass approach) for determining member temperatures, which means that the temperature is assumed uniform through the section depth. We estimate the code-based capacity (failure time) of the W8x48 perimeter column by assuming that it is a pure column with no moment. The assumption of no moment is valid since the moments that actually develop in the column are all a result of the thermal gradients, which both codes permit us to neglect. We will not consider strength reduction factors or load factors in our calculations so that we can make direct comparisons to the test results.

To calculate the time to failure (based on both the AISC and the Eurocode), we use a three step process:

- *Step 1* – We set the applied axial force P equal to the nominal capacity of the column (P_n), which considers the unbraced length and the material strength reduction factors. By setting $P = P_n$, we solve for the yield strength reduction factor $k_{y,T}$.
- *Step 2* – Both AISC and the Eurocode provide tables that correlate $k_{y,T}$ to a specific temperature, so from $k_{y,T}$ the steel temperature at failure is obtained.

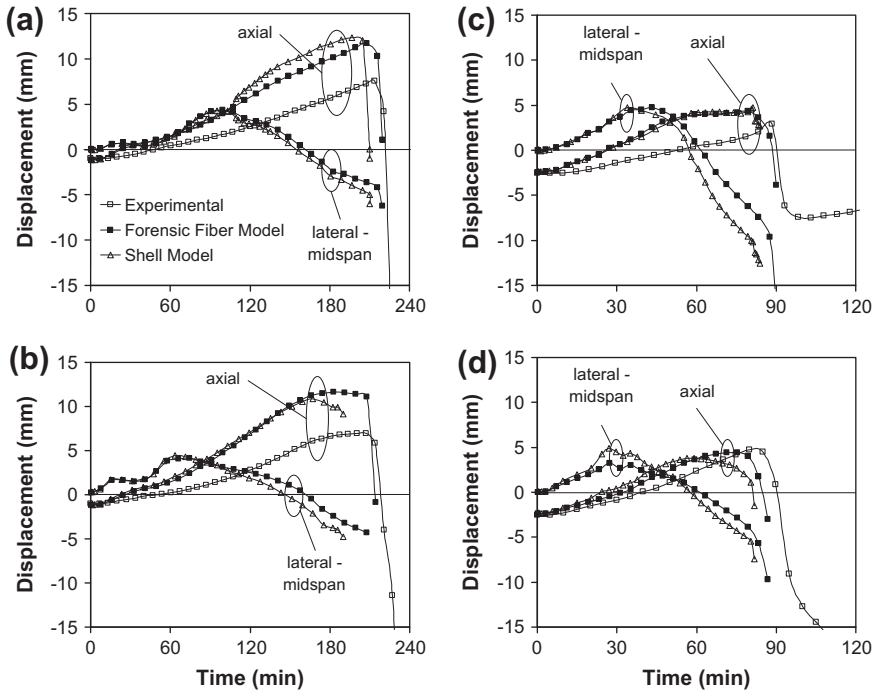

Fig. 16. Comparison of experimental, fiber-beam element, and shell-element displacements for beam–columns (a) C1-S, (b) C1-W, (c) C2-S, and (d) C2-W.

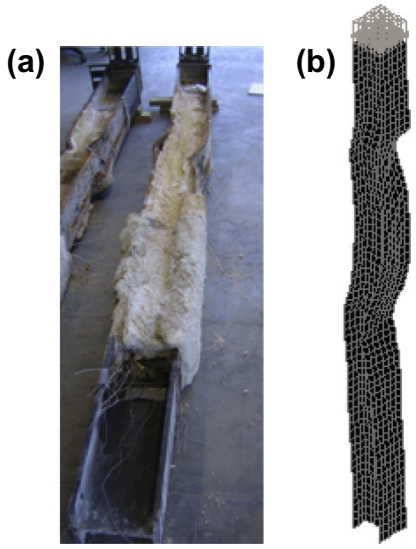

**Computational displacements are shown to scale.*

Fig. 17. Failure pattern of beam–column C1-S: (a) experimental specimen and (b) shell model.

- *Step 3* – A lumped mass heat transfer analysis is made (using a spreadsheet) assuming that the temperature of the section is the sum of two lumped mass analyses: (1) unprotected beam with fire applied only where the fire protection is missing; and (2) protected beam with fire applied everywhere except where the fire protection is missing. This was done to represent the experimental specimens shown in Fig. 3. Using the steel temperature calculated in Step 2, the time to failure is thus obtained. We also performed this step based on a two-dimensional heat transfer analysis, which is that represented by the a priori results shown in Fig. 8. Using the recording with the maximum temperature (STC1 or WTC1), we estimated the time to failure.

A summary of our findings is shown in Table 5. It is seen that the AISC and Eurocode yield similar results. When compared to the experimental results shown in Table 4, we see that the codes are too conservative for the C1-S and C1-W specimens based on the lumped mass approach. The heat transfer analysis results are a better match to the experimental but are still quite conservative due to the fact that we used the maximum temperature applied to the whole section, which is an assumption permitted by the codes. For the C2-S and C2-W specimens the lumped mass analyses are also conservative. The heat transfer analysis yields failure times that are reasonably conservative compared to the experiments.

4.5. Plastic response

Fig. 15 shows plots of P and M for the two computational models of each specimen at these locations of plasticity. The values of P and M are normalized by their corresponding yield strength (P_y) and plastic moment (M_p) at every time step. These plots also show normalized plastic P–M capacity curves that represent the section's plastic capacity and are calculated according to methods described by Garlock and Quiel [3]. The shape of these diagrams will change if the yield strength through the depth of the section changes due to a thermal gradient. Two capacity curves are shown in each plot: for $t = 0$ (i.e. just prior to fire exposure when the section is uniformly cool) and for the time of failure (which has a non-uniform temperature distribution).

The "path" of P–M combinations during fire exposure moves from the point marked $t = 0$ to that marked $t_{failure}$. The P–M behavior of all four columns in Fig. 15 shows good agreement between the forensic fiber and a priori models. The plots of normalized P–M for both computational models show the moment reversal described in Figs. 10d–13d. The significant increase in axial load ratio P/P_y was caused both by an increase in P (as shown in Figs. 10c–13c) and a simultaneous decrease in P_y. The magnitude of M/M_p was also amplified by a simultaneous decrease in plastic capacity. The coupled effects of increasing load and decreasing

capacity push the section closer to its plastic capacity until the path of normalized P and M reaches the capacity curve and the analysis ends. Therefore, Fig. 15 indicates that the plastic capacity was the failure mode since the last stable data point was on, or right next to, the P–M capacity envelope. Termination of the analysis prior to reaching the plastic P–M capacity curve would indicate a stability limit state rather than a plastic limit state.

Examination of Fig. 15 demonstrates the reasons that these columns yield at locations with the lowest moment. When the section has uniform temperature, maximum values of P/P_y (i.e. $P/P_y = 1$) can only be achieved with zero moment. When a thermal gradient develops, the plastic P–M capacity envelope subsequently shifts (to the left) and maximum values of P/P_y can only be achieved at negative values of M/M_p. Because the envelope shifts to the left, a constant P/P_y will have a larger plastic capacity for larger negative values of M/M_p. The length of each column's hottest region below the location of failure will therefore avoid yielding because it experiences greater values of negative M/M_p, and regions with smaller values of negative M/M_p above will yield first.

Note that Fig. 15 does not include plots of experimental P and M since a well-discretized thermal profile and plastic capacity of the experimental cross-section are not known, and therefore a reasonable comparison cannot be made. Rather than a comparison with experimental data, these plots are used to identify the exact mode and time of failure in the computational models. The experimental specimens are presumed to have the same failure mode as the computational models (i.e., full section yielding) because their structural behavior (see Figs. 10–13), location of failure (see Fig. 14), and the times to failure (see Table 4) are similar.

5. Fiber-beam vs. shell element models

Fig. 16 compares the axial displacement at the top-end of each column between the shell element models and the forensic fiber models as well as the experimental results. The lateral deflection at midspan is also shown for the two computational models. Experimental recordings of lateral deflection were not taken because reliable instrumentation to measure displacements or strains within the furnace was not available for this test. The deflection of the shell model shows close agreement with the experimental results and the forensic fiber model, and therefore the shell element model provides an adequate estimation of the column's structural response to non-uniform heating. Table 4 shows that the shell element models also experience similar times to failure as the fiber-beam element models and the experimental specimens.

Fig. 17 shows good agreement between the failure pattern of column C1-S and the shell element model. Both show significant flange deformation, which in the shell element model occurred just before the analysis terminated. Since the times to failure for the experimental specimen and shell model of C1-S were similar to that of the corresponding fiber-beam element models (see Table 4), it can be inferred that all experienced the same limit state of full section yield. This conclusion is also reinforced by the agreement of displacements (see Fig. 16) and failed shapes (see Fig. 14) among all cases. Analysis of the shell element model for the other three columns did not produce any significant flange deformation prior to their termination.

Table 3 indicates that for temperatures greater than about 500 °C, local buckling may develop and Fig. 8 shows that parts of the column did exceed such value. However, the limitations of Table 3 must be considered. The data in that table is based on local buckling predictions that, compared to limited experimental data, are modestly conservative [13]. Furthermore, the data is based on isolated plates with idealized boundary conditions. A recent study of high temperature plate buckling in I-shaped sections has shown that the critical buckling stress of the plates in an I-shape is larger than the plates in isolation [20]. These limitations of the data in Table 3 must be considered with the experimental displacement data and failure mode, which matched the computational results. Therefore it can be assumed that plate deformations observed in the experimental specimens occurred once the section reached full section yielding.

6. Conclusions

Three models with varying levels of complexity were used to calculate the fire-exposed response of beam–columns with thermal gradients: the *code-based* model, the *fiber-beam element* model, and the *shell* model. The code-based models are based on European and American Standards, which assume uniform temperature through the depth. Two types of fiber-beam element models were used in this study: (1) The *forensic fiber* model uses the exact thermal input and boundary conditions of reported fire tests; and (2) the a priori *fiber* model that estimates the thermal and boundary conditions. The shell element model discretizes the full cross section and length and is capable of capturing local (i.e. plate) instability. The following conclusions can be drawn from this study:

- The fiber-beam element models and the shell model are capable of sufficiently predicting the experimentally obtained response of beam–columns to fire. The fiber-beam element models accurately captured the changes in demand and capacity induced by the thermal gradient.
- The a priori fiber model also correlated well with the experimental results, which indicates that an idealized model can be used to calculate the response of steel beam–columns that develop non-uniform thermal gradients through their depth.
- A comparison between the shell model and the fiber-beam element model showed that the added computational expense and complexity of a shell model is not necessary to predict fire-exposed behavior when the failure mode is full plastic yielding.
- Thermal gradients induce bending moments due to the restraint of thermal bowing in addition to the moments due to the movement of the effective centroid (i.e. the center of stiffness) towards the cooler face [2]. Furthermore, this study confirms that the shape of the plastic P–M capacity envelope changes as the yield strength of the member varies thought its cross-section [3].
- Fire induced thermal gradients significantly affect the location of plastic hinge development for beam–columns that fully yield through their cross-section due to a combination of axial force and moment. Fire induced thermal gradients may shift the location of the emergent plastic hinge away from the location of maximum bending moment. Therefore, the aforementioned gradient-induced changes in capacity and demand experienced by the beam–column should be accounted for when calculating its response to fire.
- The approaches used by the codes to calculate the capacity of perimeter columns is too conservative compared to the experimental time to column failure and in general the codes do not predict the response satisfactorily since it does not properly consider thermal gradients.

This study is based on columns that are axially loaded at the centroid and have no lateral loads (the moment is induced entirely by the thermal gradients). Therefore, these conclusions are only applicable to the plastic section strength of I-shaped steel columns. It is possible that composite beam–columns (e.g., beams with a slab) could show some variations in behavior. These derivative

topics, along with longer (slender) columns subjected to stability effects and other applied load ratio ranges, are for future research.

The experimental and numerical studies presented above illustrate that the fire response of beam–columns is influenced by many factors including end restraint, load and fire scenarios, and fire induced thermal gradients. These factors need to be properly considered in order to trace the realistic fire response of beam–columns. While accounting for such factors can be achieved through detailed finite element analysis, this requires significant time, effort and skills. An alternative is to develop simplified design approaches by utilizing the results of intensive experimental and numerical studies, such as the ones presented in this paper and Dwaikat et al. [12]. The development of such simplified approaches for evaluating the fire resistance of beam–columns is currently underway at Michigan State University and Princeton University. A procedure of simplified methods for the analysis of steel perimeter columns (i.e. a specific type of beam–column) has been proposed and discussed in detail by Quiel [22] and Quiel et al. [23].

Acknowledgements

The research presented in this paper is co-sponsored by the National Science Foundation (NSF) (under Grant Numbers 0652282 and 0652292) and the National Institute of Standards and Technology (NIST) (under Grant Numbers 60NANB7D6120 and 60NANB7D6121). All opinions, findings, and conclusions expressed in this paper are the authors' and do not necessarily reflect the policies and views of NSF or NIST.

References

[1] Kodur VKR, Dwaikat MMS. Response of steel beam–columns exposed to fire. Eng Struct 2009;31:369–79.
[2] Garlock MEM, Quiel SE. Mechanics of wide-flanged steel sections that develop thermal gradients due to fire exposure. Int J Steel Struct 2007;7(3):153–62.
[3] Garlock MEM, Quiel SE. Plastic axial load–moment interaction curves for fire-exposed steel sections. ASCE J Struct Eng 2008;134(6):874–80.
[4] CEN. Eurocode 3: design of steel structures, Part 1.2: general rules – structural fire design (ENV 1993-1-2). Brussels: European Committee for Standardization (CEN); 2001.
[5] AISC. Steel construction manual. 13th ed. Chicago: American Institute of Steel Construction; 2005.
[6] Vila Real PMM, Lopes N, Simões da Silva L, Piloto P, Franssen J-M. Numerical modelling of steel beam–columns in case of fire – comparisons with Eurocode 3. Fire Saf J 2004;39:23–39.
[7] Lopes N, Simões da Silva L, Vila Real PMM, Piloto P. New proposals for the design of steel beam–columns in case of fire, including a new approach for the lateral torsional buckling. Comput Struct 2004;82:1463–72.
[8] Takagi J, Deierlein GG. Strength design criteria for steel members at elevated temperatures. J Constr Steel Res 2007;63:1036–50.
[9] Knobloch M, Fontana M, Frangi A. Steel beam–columns subjected to fire. Steel Constr 2008;1:51–8.
[10] Wang YC, Lennon T, Moore DB. The behaviour of steel frames subject to fire. J Constr Steel Res 1995;35:291–322.
[11] Isolatek International. CAFCO 300 guide specifications. Stanhope, NJ; 2008. <http://www.cafco.com/pdfs/CAFCO%20300%20Brochure.pdf>.
[12] Dwaikat MMS, Kodur VKR, Quiel SE, Garlock MEM. Experimental behavior of steel beam–columns subjected to fire-induced thermal gradients. J Constr Steel Res 2010;67(1):30–8.
[13] Quiel SE, Garlock MEM. Calculating the buckling strength of steel plates exposed to fire. Thin-Wall Struct 2010;48:684–95.
[14] Franssen J-M. SAFIR: a thermal/structural program for modeling structures under fire. AISC Eng J 2005;42(3):143–58.
[15] Tide RHR. Integrity of structural steel after exposure to fire. AISC Eng J 1998;35:26–38.
[16] Yang K-C, Lee H-H, Chan O. Performance of steel H columns loaded under uniform temperature. J Constr Steel Res 2006;62:262–70.
[17] Heidarpour A, Bradford MA. Local buckling and slenderness limits for flange outstands at elevated temperatures. J Constr Steel Res 2007;63:591–8.
[18] Kodur VK, Harmathy TZ. Properties of building materials. In: DiNenno PJ, editor. SFPE handbook of fire protection engineering. Quincy, MA: National Fire Protection Agency (NFPA); 2002.
[19] Carino NJ, Starnes M, Gross J, Yang JC, Kukuck SR, Prasad KR, et al. NIST NCSTAR 1-6A: passive fire protection: federal building and fire safety investigation of the world trade center disaster. Gaithersburg, MD: National Institute of Standards and Technology (NIST); 2005.
[20] Selamet S, Garlock MEM. Plate buckling strength of steel wide-flange sections at elevated temperatures. J Struct Eng ASCE 2012 [in press]: http://dx.doi.org/10.1061/(ASCE)ST.1943-541X.0000769.
[21] Banovic SW, McCowan CN, Luecke WE. NIST NCSTAR 1-3E: physical properties of structural steel. Federal building and fire safety investigation of the world trade center disaster. Gaithersburg, MD: National Institute of Standards and Technology (NIST); 2005.
[22] Quiel SE. Behavior and analysis of fire-exposed steel beam–columns that develop thermal gradient. PhD dissertation. Princeton, NJ: Princeton University; 2009.
[23] Quiel SE, Garlock MEM, Paya-Zaforteza I. Closed-form procedure for predicting the capacity and demand of steel beam–columns under fire. J Struct Eng ASCE 2011;137(9):967–76.